

Manuscript version: Author's Accepted Manuscript

The version presented in WRAP is the author's accepted manuscript and may differ from the published version or Version of Record.

Persistent WRAP URL:

<http://wrap.warwick.ac.uk/167972>

How to cite:

Please refer to published version for the most recent bibliographic citation information. If a published version is known of, the repository item page linked to above, will contain details on accessing it.

Copyright and reuse:

The Warwick Research Archive Portal (WRAP) makes this work by researchers of the University of Warwick available open access under the following conditions.

Copyright © and all moral rights to the version of the paper presented here belong to the individual author(s) and/or other copyright owners. To the extent reasonable and practicable the material made available in WRAP has been checked for eligibility before being made available.

Copies of full items can be used for personal research or study, educational, or not-for-profit purposes without prior permission or charge. Provided that the authors, title and full bibliographic details are credited, a hyperlink and/or URL is given for the original metadata page and the content is not changed in any way.

Publisher's statement:

Please refer to the repository item page, publisher's statement section, for further information.

For more information, please contact the WRAP Team at: wrap@warwick.ac.uk.

In-depth evaluation of micro-resistance spot welding for connecting tab to 18650 Li-ion cells for electric vehicle battery application

Nikhil Kumar^{1,*}, Sugumaran Minda Ramakrishnan², Kailasanathan Panchapakesan²,
Devarajan Subramaniam², Iain Masters¹, Martin Dowson¹, Abhishek Das³

¹WMG, The University of Warwick, Coventry, CV4 7AL, UK

²TVS Motor Company, Hosur, 635109, India

³Department of Mechanical Engineering, Indian Institute of Technology Delhi, 110016, India

*Corresponding author: nikhil.kumar@warwick.ac.uk

Abstract

In an automotive battery pack, many Li-ion cells are connected to meet the energy and power requirement. The micro-resistance spot welding (micro-RSW) process is one of the commonly used joining techniques for the development of cylindrical cell-based battery packs, especially for low to medium volume applications. This paper is focused on identifying the effect of influencing parameters of the micro-RSW process and developing an optimized joining solution to connect a 0.2 mm thin nickel tab to 18650 Li-ion battery cells. The effect of welding parameters including weld current, weld time, squeeze time, pre-heat current, pre-heat time, dwell time and hold time were investigated to optimize joint strength. Firstly, the welding pilot runs were conducted between Ni connector and two different thicknesses (i.e., 0.3 mm and 0.4 mm) of Hilumin coupons, representative of negative and positive terminals of 18650 cylindrical cells. Secondly, it was observed that the weld current had the most significant effect on the weld strength followed by weld time. Finally, at the optimum parameter combination, the live cell welding was conducted between the Ni tab and both positive and negative terminals of LG HG2 18650 Li-ion cells and the joints were relatively strong, no intermetallic compounds (IMCs) appeared. Weld microstructure studies provided insightful information on under-weld, good-weld and over-weld characterization and correlated with the joint strength. In addition, electrical contact resistance and temperature rise at the joint is equally important for electric vehicle battery applications. The joint performance was evaluated by analyzing the change in contact resistance and joint temperature rise when different amplitudes of current (i.e., 10 A, 20 A and 30 A) passed through the joints.

Keywords: Micro-resistance spot welding (micro-RSW), Li-ion cylindrical battery cell, Joint strength optimization, Electrical contact resistance, Joint temperature.

1. Introduction

Electric vehicles (EVs) or Hybrid/Plug-in Hybrid Electric Vehicles (HEVs/PHEVs) have either zero or lower tailpipe emissions than the traditional fossil fuel-based vehicles which make them greener, cleaner, and better for the environment by reducing the emission of greenhouse gases [1, 2]. Due to favourable attributes of Lithium-ion (Li-ion) batteries such as longer lifespan, higher densities of energy/power, and portability, they are extensively used to build battery packs for EVs/HEVs/PHEVs [3, 4]. Based on the energy/power/driving range requirements of an automotive battery pack, a large number of Li-ion cells are connected within battery packs. For example, cylindrical cells, one of the commonly used cell formats to build automotive battery packs, are used by several automotive original equipment manufacturers (OEMs) including Tesla, BMW and Hyundai HEVs [5]. Therefore, up to several thousand cylindrical cells must be connected in series/parallel to create suitable battery packs for the required voltage and amperage to deliver the power and driving ranges. In general, the cylindrical cell-based battery pack is composed of several battery modules and those modules are built using individual cells which need tab-to-cell terminal connections. **Fig. 1** shows a configuration of cylindrical cells to build the module from individual cells and several modules to build the pack. These tab-to-terminal connections demand efficient and cost-effective joining processes of which laser [6-9], micro-TIG [10] or resistance spot welding (RSW) [11, 12] process can be used to weld a tab to the cell terminal. In general, the RSW is emerging as an attractive joining solution due to its low maintenance and investment cost as well as meets the market demands for low to medium volume applications, such as e-bikes, two-wheelers, or e-rickshaws [13].

The main joint characteristics which are to be satisfied for the battery tab and cell terminal connections are the properties of the joint such as low electrical resistance and good mechanical strength. Improper joint might result in higher electrical resistance which will lead to excessive Joule heating [14]. Therefore, for low to medium volume applications (e.g., two-wheeler, e-rickshaw and small EV battery pack), the aim is to choose the low-cost joining processes to meet industrial needs of the OEMs as well as small and medium-sized enterprises (SMEs). Additionally, the joining process should satisfy dissimilar materials joining needs. Therefore, considering the aforementioned requirements, the RSW is one of the most suitable welding processes [12], and additionally, it does not need high capital investment and skilled operators. In the present work, the micro-RSW process is used for joining lithium-ion cells, typically used for portable devices and vehicles applications [5, 11], due to low investment cost, shorter process time, localized heat, low electrical contact resistance, and better corrosion resistance

[5]. Micro-RSW usually requires a low weld current as well electrode force compared to that of the normal resistance spot welding. Therefore, the amount of heat generated during the welding process is small and does not affect cell components. In between all four micro-RSW configurations (opposed, series, parallel and step) [13, 15], the series spot weld head is the only feasible configuration for welding the tab to Li-ion cell terminals as the series weld doesn't require access to the bottom part as well as two weld nuggets are produced using two electrodes.

In general, the battery tab materials shall be electrically and thermally conductive to minimize power loss and maximize heat dissipation. There are various metals such as nickel, copper, electrical grade steel, aluminum, which have good electrical and thermal conductivity and are found to be suitable for the battery tab. The battery tab material is also selected based on parameters such as cost, compatibility with cell terminal materials, corrosive properties, welding process and good tensile as well as fatigue properties. Commercially available 18650 lithium-ion cell casings are mostly made of nickel-plated steel (e.g., Hilumin) [16] and 0.2 mm nickel is selected as a tab material because of their good corrosion properties, good compatibility/weldability with battery terminal material (i.e., nickel-plated steel).

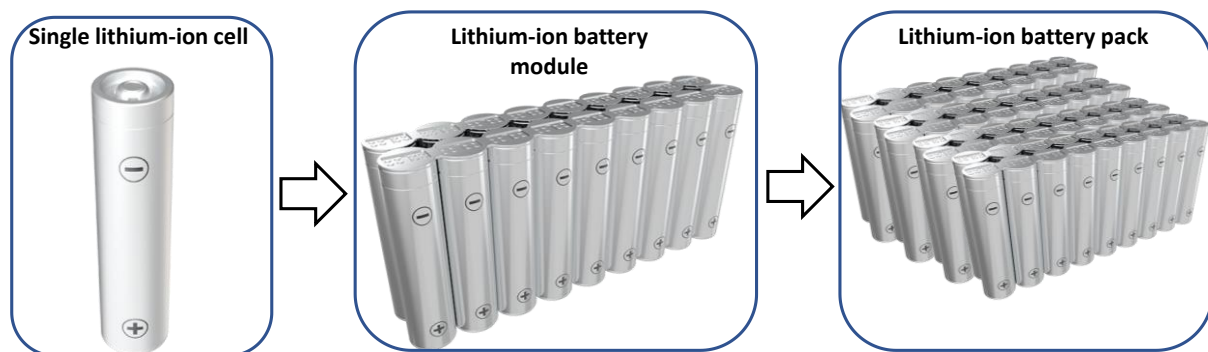


Fig. 1. Hierarchical steps to build battery pack from lithium-ion cells [3]

In the work of Dong et al. [17], the electrode sticking mechanism and factors affecting the sticking, including welding current, weld time, electrode tip coating, electrode force and electrode spacing, were studied during micro-resistance welding of very thin nickel-plated steel to nickel sheets in the assembly of a cell-phone battery package. They were found that electrode sticking was caused by local metallurgical bonding between the electrode and the nickel-plated steel sheet. They reduced electrode sticking by reducing welding current and weld time and increasing electrode force and electrode spacing. Masomtop et al. [13] studied the effects of influencing parameters in the series/parallel gap spot welding process and determine the optimized parameters setting for spot welding between 18650 Li-ion battery cells and

Hilumin/Nickel sheet metal connectors. They concluded that a slot on the connecting tab can make more electric current flow through the nuggets and for choosing the connecting tab material, the temperature and the electric current using nickel tab is higher than using Hilumin at the same stage of the maximum supply voltage. Although, Ni tab to Hilumin joints are reported in the literature [13, 17], however, the process parameters weren't optimized to achieve high joint strength. Furthermore, the weld nuggets cross-section analysis was not conducted to check the fusion zone morphology, which is essential for battery joining which are included in the current study. Also, Rikka et al. [18] were conducted the micro-resistance spot welding on their fabricated cylindrical lithium-ion cell where they used nickel anode tab to weld with the inner aluminium casing of the cell. They have adopted Taguchi's design of experiment for micro-RSW parametric optimization of high electrically conductive nickel-to-aluminium joints. They were concluded that the aluminium casing can be used to fabricate high-energy density cylindrical lithium-ion cells for EV applications. In another work, micro-RSW of 0.2 – 0.5 mm thickness Kovar, steel, and nickel using different types of power supply were investigated by Ely and Zhou [19]. The effects of process parameters (welding current/pulse energy, electrode force, and welding time/pulse width) on joint strength and nugget diameter were studied. They have concluded that the Kovar and steel are readily micro resistance welded because they require lower welding current and show decreased electrode–sheet sticking. Whereas, micro resistance welding of nickel is relatively problematic because the nickel requires higher welding current or pulse energy and shows increased electrode–sheet sticking. In another study by Kumar et al. [20], micro-RSW was used to join ultra-thin Inconel 718 to stainless steel 410 and they observed that welding current and welding time were the most influential parameters affecting the joint strength. Similar to this, Baskoro et al. [21] studied the effects of micro-RSW parameters on the quality of weld joints on aluminium thin plate AA 1100. They have used an alternating current (AC) RSW machine for welding purposes and found for the tensile shear test that by increasing the electrode force, the load rate would be decreased.

Within the scope of the literature review, it was observed that the in-depth analysis of micro-RSW joining of 0.2 mm Ni connecting tab to 18650 battery cell terminals within a battery module assembly has not been fully investigated. A detailed analysis is needed for micro-RSW joints in terms of joint strength and electrical contact resistance. In addition, the temperature rises at the micro-RSW joint due to the application of a charge/discharge current is also necessary to avoid undesired outcomes such as joint failure or thermal runaway [22].

Therefore, this paper addresses the following objectives:

- To determine the preferred micro-RSW process parameters to achieve the maximum joint strength for nickel tab to cylindrical cell terminals
- To investigate the joint microstructure, analyse defects and correlate to the joint strength
- To correlate electrical resistance of micro-RSW welded coupon combinations with the temperature rise at the joint due to the application of charge/discharge current.
- To estimate the safe value of passing current to live cell welded battery for industrial application.

The remainder of this paper is arranged as follows: Section 2 provides the details of the experimental set up and procedure including materials, micro-RSW joint preparation, and set-ups for mechanical, electrical and thermal characterization; the results and discussions are made in Section 3; and conclusions are drawn in Section 4.

2. Experimental setup and procedure

The focus of the present work is to join the nickel tab to LG HG2 18650 cylindrical cell terminals. As the thicknesses of the cylindrical cell negative and positive terminals are 0.3 mm and 0.4 mm respectively, experimental investigations were conducted in lap joint configuration to weld 0.2 mm Ni tabs to 0.3 and 0.4 mm Hilumin [23] (equal to the thickness of the cell terminals) and corresponding chemical compositions are given in **Table 1**. Thereafter, joint strength, metallurgical analysis with electrical and thermal performances were conducted. Subsequently, the optimized process parameters were utilized to weld the Ni tab to live cells.

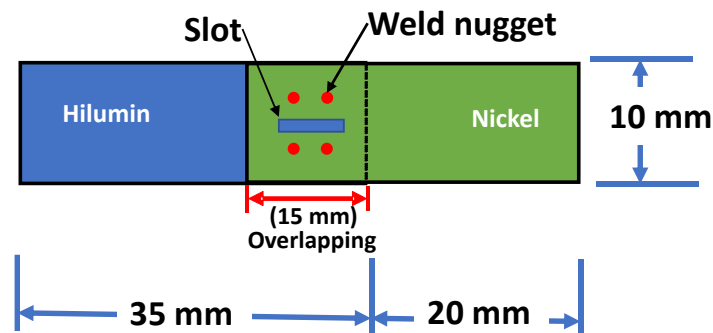


Fig. 2. Schematic diagram of 0.2 mm Ni tab to 0.3/0.4 mm Hilumin micro-RSW

In this study, a 0.2 mm Ni slotted tab (upper tab) was welded to 0.3 mm and 0.4 mm Hilumin (lower tab) in a lap joint configuration as shown in **Fig. 2** with the specimen dimensions. The

slot was used to direct the current flow between tab and battery terminal avoiding shunting current path within the parent Ni material [13].

Table 1. Details of materials used in this study [24, 32]

Material	Thickness (mm)	Chemical composition (wt.%)
Hilumin / 18650 Li-ion battery CAN material	0.3 /0.4	C = 0.047, Mn = 0.235, P = 0.011, S = 0.010 Al = 0.059, Si = 0.002, Bo = 0.0019 Fe-balance
Nickel (Ni)	0.2	Ni > 99, Mn < 0.35, Cu < 0.25, Si < 0.35, C < 0.15, S < 0.01, Fe < 0.40, other balance

Typically, the tab without a slot needs higher current amplitude, resulting in a burn mark in the middle area between two weld spots and high wear of electrode tips [25, 26]. Micro-RSW was conducted using a MacGregor RSW machine having maximum output current flow of 6000 Amps DC with current/voltage/power control mode (Make: MacGregor; Model: M31 Smart Series). A 3.0 mm diameter domed-shaped electrodes were used and they were made of aluminium dispersed copper (Cu content around 98.9%) without water or air cooling as the application was intended for micro-RSW for thin sheet. Electrode's superior strength retention, thermal and electrical conductivities (80% IACS i.e., International Annealed Copper Standard) were higher than conventional copper alloys which made them more suitable for the micro-RSW process [27, 28]. For the electrode tip geometry, the domed electrode tip was better than the other electrode tip geometries (e.g., flat and tapered) in terms of the electrode's life span and oxidation [13].

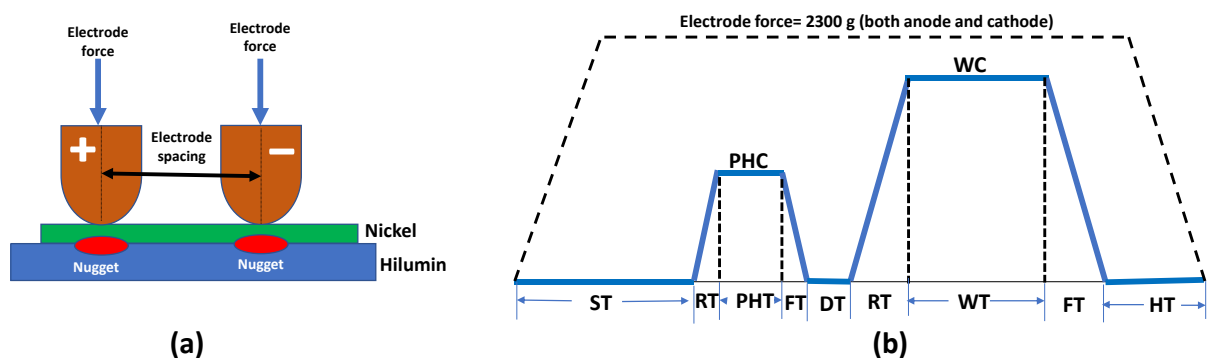


Fig. 3. Schematic diagram (a) welding set up and (b) welding current profile [where, ST= squeeze time, RT- rise time, PHC= pre-heat current, PHT= pre-heat time, FT= fall time, DT- dwell time, WC= weld current, WT= weld time, HT= hold time]

The schematic diagram of the welding setup and the welding current flow profile is given in **Fig. 3(a)** and **(b)** respectively. Electrode sticking tests were performed on coupons and an electrode force of 2300 g was applied on each electrode when the electrode force decreased from 2300 g the electrode sticking was observed due to high contact resistance between the electrode tip and upper surface of the top sheet. Also, if the electrode force was too low, excessive heat production can lead to the formation of a few local metallurgical bonds at the beginning of the welding cycle but are not sufficient to cause a measurable sticking force [17]. The limits of welding parameters (e.g., weld current, weld time, squeeze time, pre-heat current, pre-heat time, dwell time and hold time) were selected based on the pilot experimental trials. The RSW process parameters were optimized in two stages.

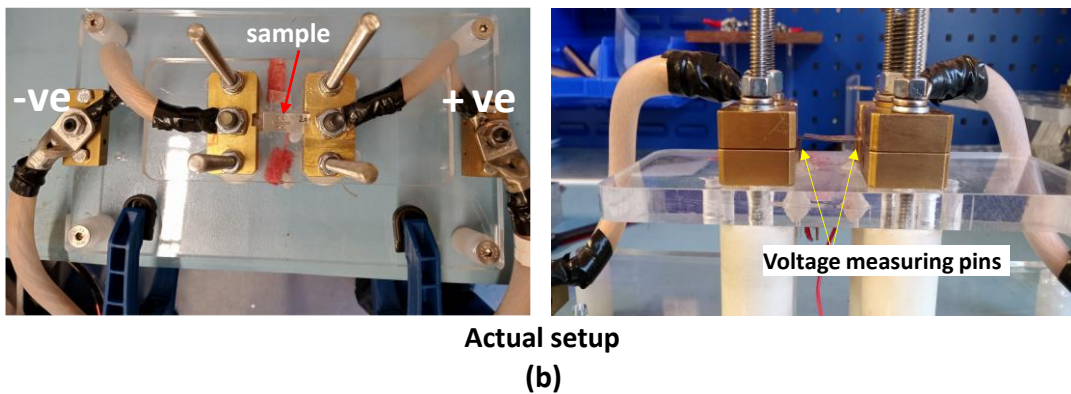
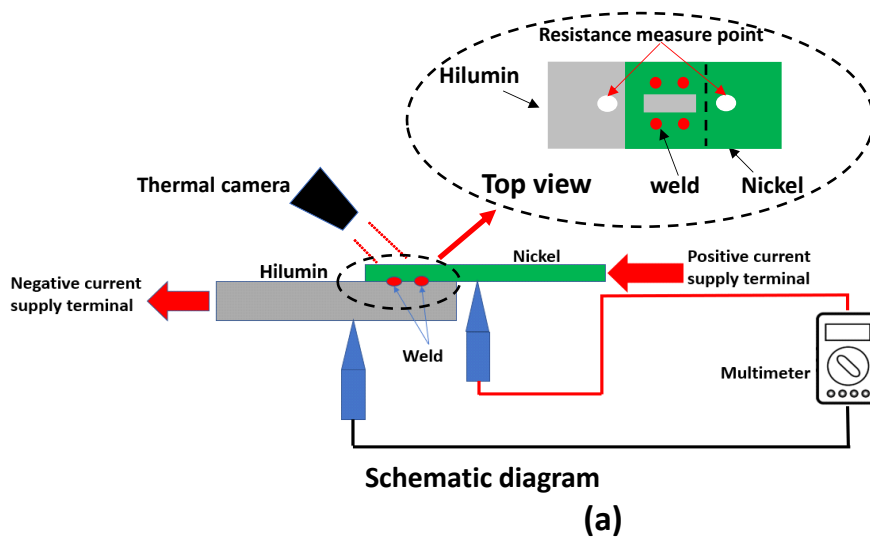


Fig. 4. Resistance and temperature at joint measurement (a) schematic diagram and (b) actual experimental set-up [32]

Firstly, the significant process parameters and their limits were identified using a hybrid Taguchi's-analysis of variance (ANOVA) analysis with 2 nuggets welding. Secondly, a full factorial design of experiment (DOE) with 4 nuggets was conducted to optimize the obtained

significant process parameters, namely, weld time and weld current in terms of maximum load (i.e., peak load obtained from the load vs grip displacement plot from lap shear test) to achieve a good quality weld. The 4 nuggets weld was advantageous to improve the electrical conductivity and mechanical strength by increasing the contact area between the connecting tab and battery cell terminal. Subsequently, peel strength was also evaluated for the live cell welds at optimized parameters as peel also commonly occurred in failure mode. Lap shear tests were conducted on an Instron 3367 test frame with a 1 kN load cell and a crosshead speed of 2 mm/min. Whereas, the peel strength of the live cell welded samples were conducted using ZWICK Z100 tensile testing machine equipped with a climate chamber for avoiding any accident due to electrolyte leakage. For microstructural evaluation, a precision cutter Isomet 500 was used to cut the specimens to minimize deformation formed during cutting. Cut specimens were then mounted in Bakelite and mechanically polished using #1200 SiC paper, 9 μm , 3 μm and 1 μm metadi supreme diamond suspension and 0.05 μm colloidal silica. Specimens were etched using 2% Nital for 4 seconds to reveal the microstructure. Consequently, microstructure examination (weld bead geometry) was analysed under an optical microscope (Make: Nikon; Model: LV150N). Field emission scanning electron microscope (FE-SEM) equipped with an energy dispersive X-Ray analysis (EDX) system was used for microstructural analysis. For measurement of the resistance of the welded coupons specimens, the four-point probe measurement technique [29-32] was applied in order to reach a high level of accuracy. For example, Hu et al. [33] used the same techniques for measuring the contact resistance of the faying surface of the resistance spot welding process. Similarly, Brand et al. [12] and Solchenbach et al. [34] also used the four-point probes method for calculating the electrical resistance of the welded joints. In the present work, the same method was adopted to measure the electrical contact resistance and corresponding temperature rise. Electrical current was passed through the welded Ni to Hilumin and the voltage drop was measured across the weld as shown in **Fig. 4(a)** schematically. Resistance was calculated by application of Ohm's law ($V = IR$), from the induced voltage due to the application of the current. When the current was supplied, resistive heat loss ($I^2 R_{\text{weld}}$) increased the temperature at the welded location. To measure the rise in temperature a thermal camera was used. The actual configuration of the testing setup is given in **Fig. 4(b)**. A polyamide tape, also known as Kapton tape, was used to cover the welded area (i.e., thermal camera temperature measuring/focused area) to set the emissivity close to 1 and eliminate the effect of changing emissivity due to temperature increase. The emissivity from black paint and polyamide tape are almost the same. In addition, Kapton tape has a wider temperature range that can be used

for hot surfaces within its upper-temperature limit. A similar approach was used by Kumar et al. [32] on the top of the measuring surface to set the emissivity close to 1 for various combinations of laser welded samples. The increase in temperature at the weld was essential to evaluate because of safety. The tab was connected to the battery cells casing (contained electrochemically active material) where temperature-sensitive materials inside the cell limit the maximum heat input (**Fig. 1**). Therefore, a thermal camera (make: Optris PIX Connect; model: Xi400) was fixed on the top and focused on the weld during the resistance measurement displayed in **Fig. 4(a)**. A rigid fixture was used to ensure an identical positioning of the voltage measuring pins with respect to the samples.

3. Results and discussions

3.1. Identifying significant micro-RSW process parameters

In this experiment, RSW welding of 0.2 mm Ni tab to 0.3 mm Hilumin with two nuggets was conducted in the lap joint configuration. The process parameters selected from the welding schedule (**Fig. 3b**), for investigation were WC, WT, ST, PHC, PHT, DT and HT and their limits are presented in **Table 2**, whilst RT and FT were fixed at 1 ms. The limiting value of the process parameters was selected by initial screening experiments. Thereafter, Taguchi design matrix was developed for the experimental trials within the limiting value of the process parameters and the ANOVA technique was used to find the significance of input parameters in terms of percentage contribution on response. Taguchi design matrix and the measured values of average maximum load (ML)/peak load and associated standard deviation were given in **Table 3**. Each experiment was performed three times and the average values of ML are reported.

Table 2. Process parameters used to produce the welds

Parameters (notation), unit	Levels		
	1	2	3
Squeeze time (ST), ms	50	100	150
Pre-heat current (PHC), A	800	1000	1200
Pre-heat time (PHT), ms	0.5	1.5	2.5
Dwell time (DT), ms	3	6	9
Weld current (WC), A	1200	1600	2000
Weld time (WT), ms	2	5	8
Hold time (HT), ms	100	200	300

The weld quality was arbitrated based on ML value. The maximum and minimum peak loads were obtained from sample no. 9 (578.13 N) and sample no. 4 (36.41 N) respectively. The RSW welded samples of experiments no. 4 and 9 were given in **Fig. 5(a)** and **(b)** respectively. The results obtained from the analysis-of-variance (ANOVA) were plotted in the pie chart format as shown in **Fig. 6(a)**. From **Fig. 6(a)**, it was found that the weld current (66.22%) has the most significant effect on the ML followed by weld time (27.99%). **Fig. 6(b)** shows the effect of RSW process parameters in ML using mean effect plots. It is evident from **Fig. 6(b)** that ML increases significantly with increasing weld current and weld time, whilst other parameters such as ST, PHC, PHT, DT, WC, WT and HT have insignificant effects on ML.

Table 3. Process parameters and their levels as per Taguchi's design

Exp. no.	Parameters							Response
	ST (ms)	PHC (A)	PHT (ms)	DT (ms)	WC (A)	WT (ms)	HT (ms)	ML (N) \pm SD
1	50	800	0.5	3	1200	2	100	80.13 \pm 8.41
2	50	800	0.5	3	1600	5	200	307.15 \pm 16.43
3	50	800	0.5	3	2000	8	300	527.26 \pm 36.54
4	50	1000	1.5	6	1200	2	100	36.41 \pm 7.01
5	50	1000	1.5	6	1600	5	200	305.89 \pm 17.09
6	50	1000	1.5	6	2000	8	300	543.84 \pm 30.21
7	50	1200	2.5	9	1200	2	100	80.14 \pm 9.91
8	50	1200	2.5	9	1600	5	200	351.93 \pm 26.04
9	50	1200	2.5	9	2000	8	300	578.13 \pm 12.68
10	100	800	1.5	9	1200	5	300	117.23 \pm 25.67
11	100	800	1.5	9	1600	8	100	350.27 \pm 10.59
12	100	800	1.5	9	2000	2	200	280.09 \pm 6.82
13	100	1000	2.5	3	1200	5	300	123.09 \pm 18.42
14	100	1000	2.5	3	1600	8	100	401.21 \pm 12.30
15	100	1000	2.5	3	2000	2	200	298.36 \pm 5.01
16	100	1200	0.5	6	1200	5	300	135.73 \pm 5.28
17	100	1200	0.5	6	1600	8	100	366.10 \pm 21.48
18	100	1200	0.5	6	2000	2	200	260.15 \pm 22.04
19	150	800	2.5	6	1200	8	200	158.95 \pm 7.97
20	150	800	2.5	6	1600	2	300	154.01 \pm 0.75
21	150	800	2.5	6	2000	5	100	421.43 \pm 5.26
22	150	1000	0.5	9	1200	8	200	152.12 \pm 12.68
23	150	1000	0.5	9	1600	2	300	145.11 \pm 14.10
24	150	1000	0.5	9	2000	5	100	404.25 \pm 25.14
25	150	1200	1.5	3	1200	8	200	159.51 \pm 10.11
26	150	1200	1.5	3	1600	2	300	158.91 \pm 7.02
27	150	1200	1.5	3	2000	5	100	441.89 \pm 5.28

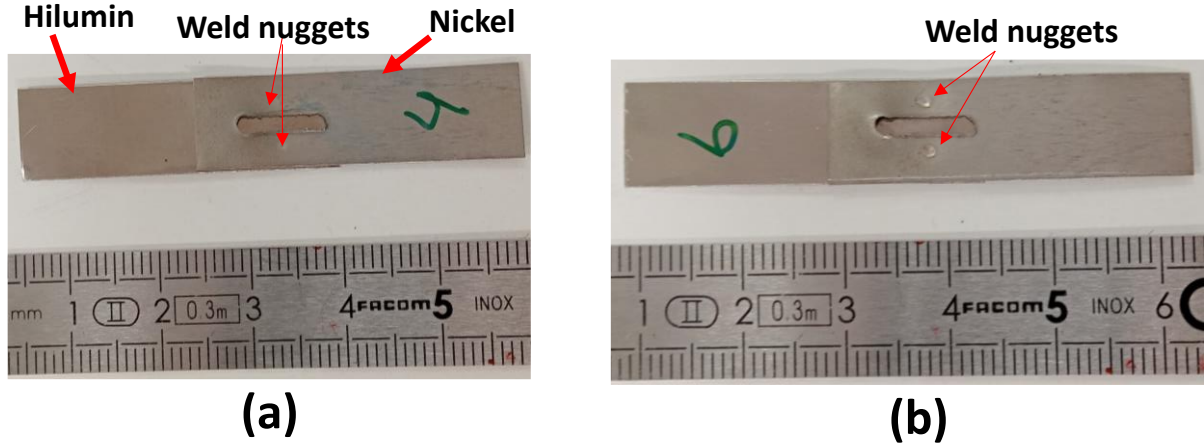


Fig. 5. RSW welded samples (a) experiment no. 4 (minimum ML) and (b) experiment no. 9 (maximum ML)

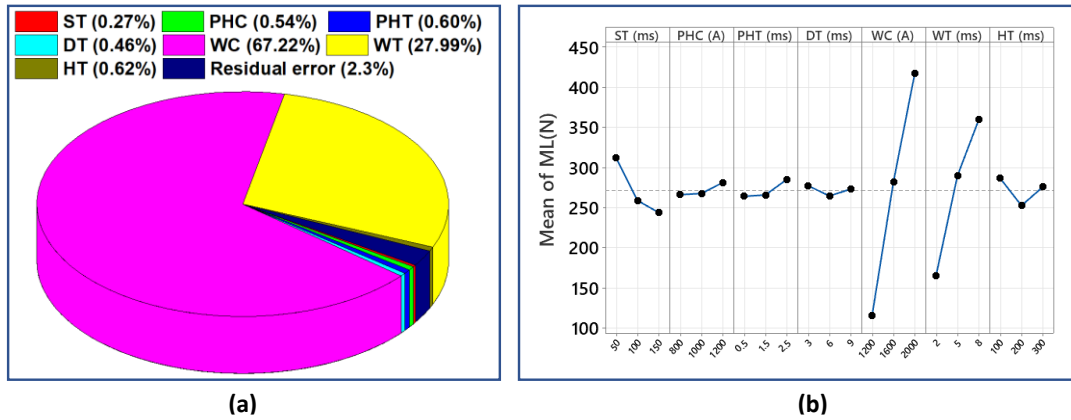


Fig. 6. (a) percentage contribution of process parameters and (b) effect of process parameters on maximum load (ML)

Therefore, the WC and WT would be considered as a process parameters for the further design of experiment study, and other parameters will be fixed at a level value in which the maximum mean value was obtained (**Fig. 6b**). In the case of high WC and WT, more energy is available to melt the materials. Due to the increase in heat input, the weld nugget size was increased and subsequently, produced deeper penetration depth and wider interface width which resulted in higher joint strength.

3.2. Identifying the effects of the significant process parameters

This section describes in detail the effects and optimization of RSW process parameters (weld current and weld time - most significant process parameters) through the mechanical, microstructural and statistical approaches to weld the negative and positive terminals of live cells. The selection of process parameters was done based on the foregoing pilot studies and their significance. The design of experiment was made considering full factorial design for both

the 0.2 mm Ni to 0.3 and 0.4 mm Hilumin joints considering 4 nuggets. The selected process parameters and their limits for welding the 0.2 mm Ni to 0.3 mm Hilumin were given in **Table 4**. Weld current (WC) and weld time (WT) were considered as varying process parameters and other parameters (ST, PHC, PHT, DT and HT) were kept constant. Each experiment was performed three times and experimental runs with their corresponding average values of ML are reported in **Table 5**. Finally, the optimization was conducted using a full factorial design. The minimum and maximum load were obtained from experiment no. 1 (WC= 1400 A; WT= 4 ms) and 36 (WC= 2400 A; WT= 14 ms) respectively. In addition, the expulsion phenomenon does not appear in the limiting range of process parameters (i.e., WC and WT), which is recommended for the micro-RSW process. The welding cross-sections were examined at relatively low magnification such that the whole weld zone geometry could be observed. The cross-sectional images of the weld nuggets for the minimum (experiment no. 1) and maximum (experiment no. 36) load samples were shown in **Fig. 7(a)** and **(b)** respectively. Several researchers [35-37] agreed that the performance of the micro-RSW weld was strongly influenced by the size of the nugget and the nugget mechanical properties, in which case welding failure occurred. Both the nugget size and mechanical properties of the welds were directly affected by welding parameters, such as welding current and welding time, as shown in previous sections. **Fig. 8** shows the mean effect plots and response surface plots to determine the effect of input parameters on ML. From **Fig. 8(a)**, it was found that the WC has the most significant and positive effect on maximum load followed by WT. **Fig. 8(b)** shows the interaction effect of WC and WT on ML. It was found that the ML was increased with increasing WC and WT, and the ML was maximum at a higher value of WC and WT. This effect is caused by the increase in the nugget diameter with weld current and weld time, as shown in **Fig. 9**. This is due to the fact that the high heat input applied at the faying surface for the higher value of WC and WT, resulting in a large nugget diameter and thus, a good joint. **Fig. 9** shows the failure mode, from the results of the static peel tests for the lower, intermediate and higher values of WC and WT (i.e., Exp. no. 1, 13, 15, 23, 31, 33, 35 and 36). From **Fig. 9**, nugget diameters lie between (0.585 – 1.78 mm), minimum nugget diameter was obtained for exp.no. 1 and maximum for exp. no. 36. The failure modes observed in the tests can be divided into three categories interfacial failure modes (i.e., **Fig. 9a**), pull-out failure mode (i.e., **Fig. 9c – h**) and both modes of failure (i.e., **Fig. 9b**). The interfacial failure mode occurs for nugget diameter 0.585 mm (**Fig. 9a**) while pull-out failure mode happened for nugget diameters above 1.05 mm (**Fig. 9c – h**). For nugget size 0.648 mm (**Fig. 9b**) both modes of failure coexist.

Table 4. Process parameters and their limits

Varying parameters	Levels						Fixed process parameters
	1	2	3	4	5	6	
WC (A)	1400	1600	1800	2000	2200	2400	ST= 50 ms; PHC= 1200 A; PHT= 2.5 ms; DT= 3 ms; HT= 100 ms;
WT (ms)	4	6	8	10	12	14	

Table 5. Process parameters and their limits as per full factorial design used to produce weld

Exp. no.	WC (A)	WT (ms)	ML (N) \pm SD
1	1400	4	389.65 \pm 4.08
2		6	466.03 \pm 42.21
3		8	493.86 \pm 11.57
4		10	675.83 \pm 39.25
5		12	560.96 \pm 28.16
6		14	633.09 \pm 21.21
7	1600	4	497.05 \pm 26.16
8		6	690.55 \pm 29.83
9		8	775.71 \pm 39.47
10		10	778.72 \pm 23.36
11		12	759.06 \pm 43.39
12		14	745.47 \pm 11.79
13	1800	4	655.37 \pm 35.08
14		6	857.18 \pm 24.54
15		8	796.33 \pm 70.22
16		10	798.71 \pm 17.02
17		12	889.06 \pm 24.90
18		14	984.97 \pm 42.04
19	2000	4	772.34 \pm 36.80
20		6	892.95 \pm 16.42
21		8	937.45 \pm 13.70
22		10	1012.05 \pm 30.13
23		12	1071.90 \pm 13.41
24		14	1081.92 \pm 28.34
25	2200	4	819.52 \pm 34.99
26		6	890.43 \pm 99.26
27		8	1001.60 \pm 38.70
28		10	1059.92 \pm 10.34
29		12	1076.64 \pm 11.20
30		14	1081.71 \pm 13.49
31	2400	4	890.12 \pm 47.33
32		6	928.79 \pm 69.88
33		8	1007.87 \pm 53.12
34		10	1053.57 \pm 4.48
35		12	1065.43 \pm 3.80
36		14	1082.26 \pm 0.43

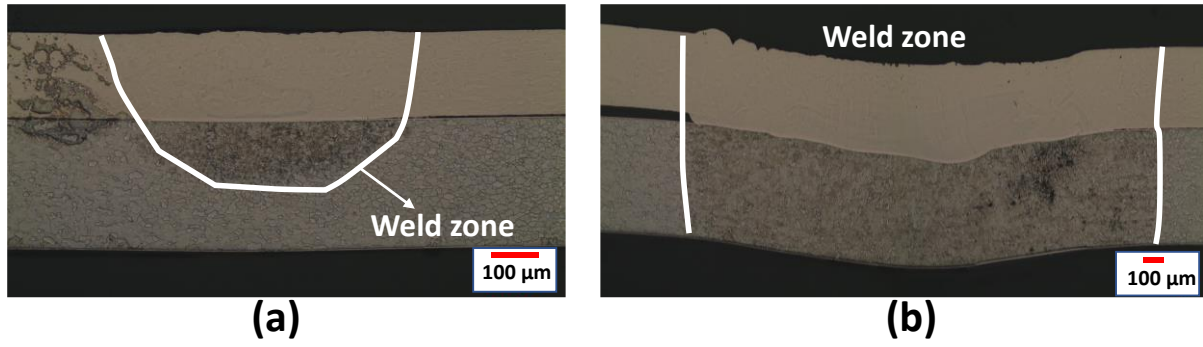


Fig. 7. Cross-sectional view of the weld nugget (a) for the minimum load (experiment no. 1) and (b) maximum load (experiment no. 36)

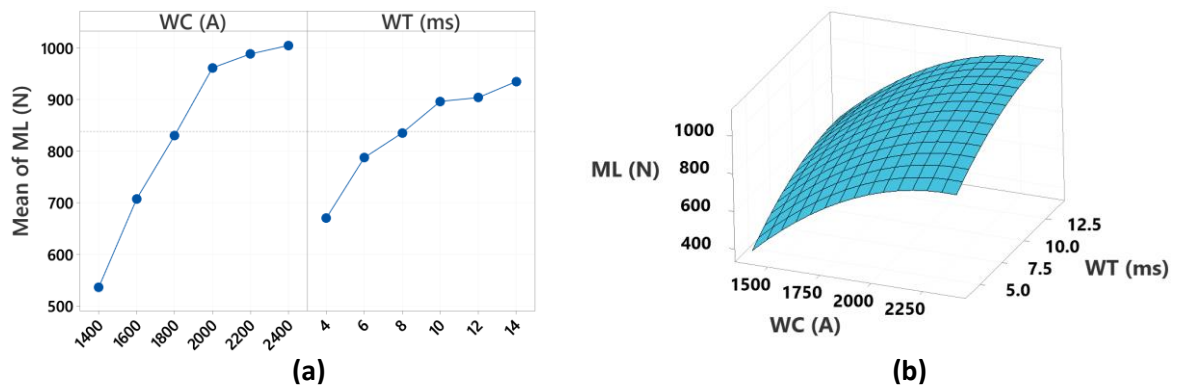


Fig. 8. Effect of process parameters (a) mean effect plots for ML and (b) response surface plot

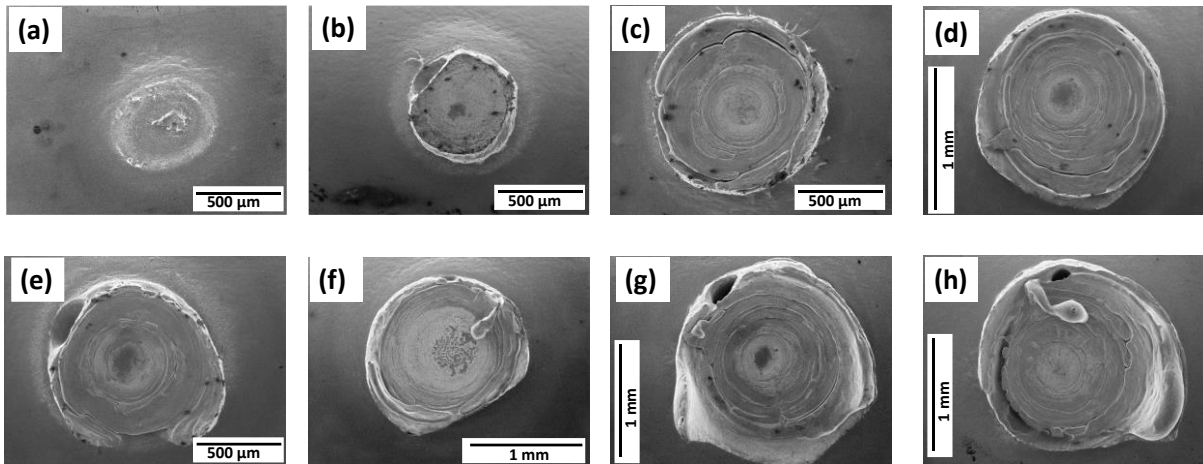


Fig. 9. Variation of failure mode with process parameters (a) WC= 1400A, WT= 4ms (b) WC= 1800A, WT= 4ms (c) WC= 1800A, WT= 8ms (d) WC= 2000A, WT= 12ms (e) WC= 2400A, WT= 4ms (f) WC= 2400A, WT= 8ms (g) WC= 2400A, WT= 12ms and (h) WC= 2400A, WT= 14ms

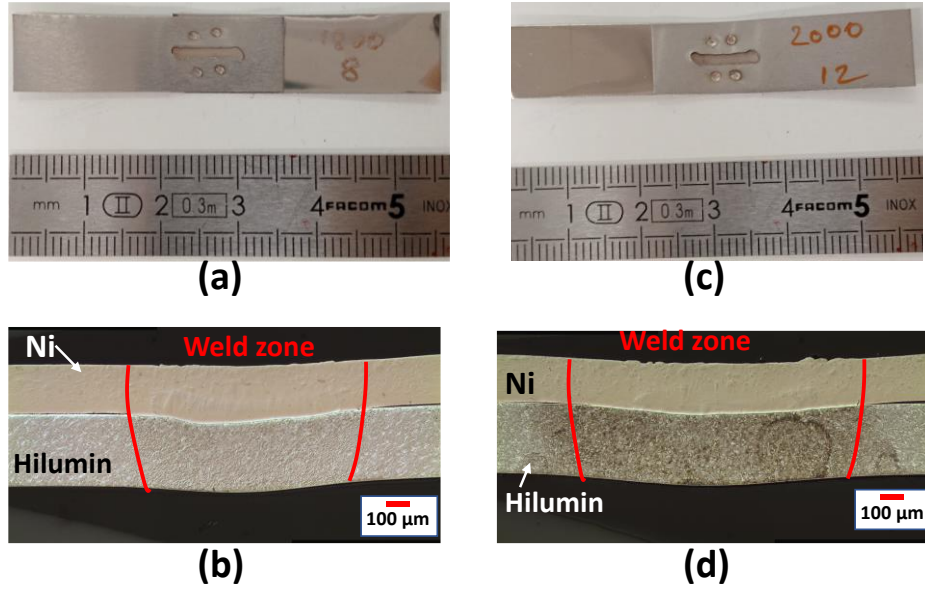


Fig. 10. Micro-RSW sample and an area of molten and subsequently solidified metal at (a, b) WC= 1800 A; WT= 8 ms and (c, d) WC= 2000 A; WT= 12 ms

In order to achieve the reliability of the welds, the welding parameters should be adjusted so that pull-out failure mode is obtained during testing. The pull-out failure modes were observed for the parametric combination above 1800 A weld current and 8 ms weld time, as is illustrated in **Fig. 9**. Therefore, the WC of 1800 A and weld time of 8 ms was considered as the lower limit of the optimum parameter setting. Mostly, a small increase/decrease in the maximum load was observed (**Table 5**) above the parameter combination of 2000 A weld current and 12 ms weld time. This might be associated with the minor change in diameter of the nugget with increasing weld current and weld time. Hence, the WC of 2000 A and WT of 12 ms were selected as the upper limiting value of the optimized parameter to achieve the maximum ML value. Also, there was a tendency for top surface burn, spatter, and porosity for the higher values of WC and WT. Thus, the ‘preferred-weld’ process parameters range for the 0.2 mm Ni to 0.3 mm Hilumin joints were determined as WC of (1800 – 2000 A) and WT of (8 – 12 ms).

Fig. 10(a, b) and **(c, d)** show the micro-RSW welded samples and a cross-sectional image of molten and subsequently solidified metal at the lower (WC= 1800 A; WT= 8 ms) and higher (WC= 2000 A; WT= 12 ms) value of preferred parameters set respectively. In addition, the temperature at the joints during welding increases with increasing WC and WT, and in the case of live cell welding, high temperature produced at cell terminals can accelerate ageing and promote solid electrolyte interface growth leading to premature failure [38-40]. Also, bending of the cell terminal material is not ideal for battery application as it can produce cracks leading to electrolyte leakage or potential thermal runaway. This emphasises the importance of

controlling WC and WT for low thermal input. It can be observed in **Fig. 10(d)** that very small bottom material bending was obtained as compared to **Fig. 7(b)** for experiment no. 36. Similarly, 0.2 mm Ni to 0.4 mm Hilumin (cell positive terminal representative material) sheets were welded and analyzed. The measured value of ML obtained from the universal testing machine (Instron) from the welded samples at different values of WC and WT were given in **Table 6**. The limiting value of the process parameters for 0.2 mm Ni to 0.4 mm Hilumin was decided on the basis of the optimized results obtained from the 0.2 mm Ni to 0.3 mm Hilumin combination. The WC and WT were varied for 6 and 2 different levels respectively. The minimum (935.75 N) and maximum (1255.40 N) values of ML were obtained for experiments no. 1 and 12 respectively.

Table 6. Process parameters and their limits and the measured value of maximum load

Exp. no.	WC (A)	WT (ms)	ML (N) \pm SD
1	1800	8	935.75 \pm 10.37
2	1900		1000.64 \pm 17.68
3	2000		1009.88 \pm 46.01
4	2100		1135.37 \pm 16.40
5	2200		1132.83 \pm 35.62
6	2300		1109.50 \pm 38.28
7	1800	12	1048.95 \pm 11.60
8	1900		1101.18 \pm 11.76
9	2000		1136.79 \pm 16.47
10	2100		1222.15 \pm 8.71
11	2200		1245.29 \pm 39.68
12	2300		1255.40 \pm 12.32

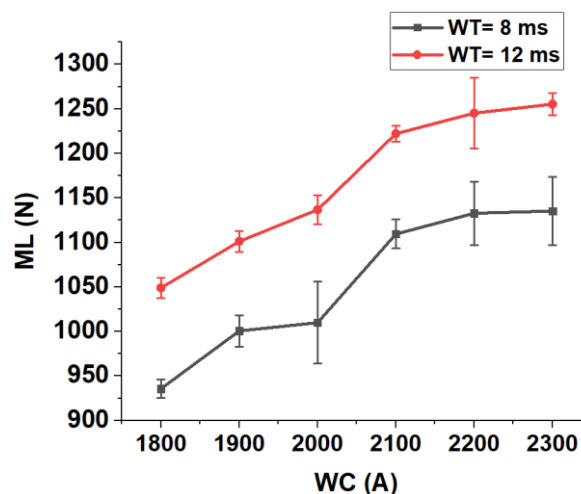


Fig. 11. Effect of weld current (WC) on maximum load (ML) whilst weld time were fixed at 8 and 12 ms

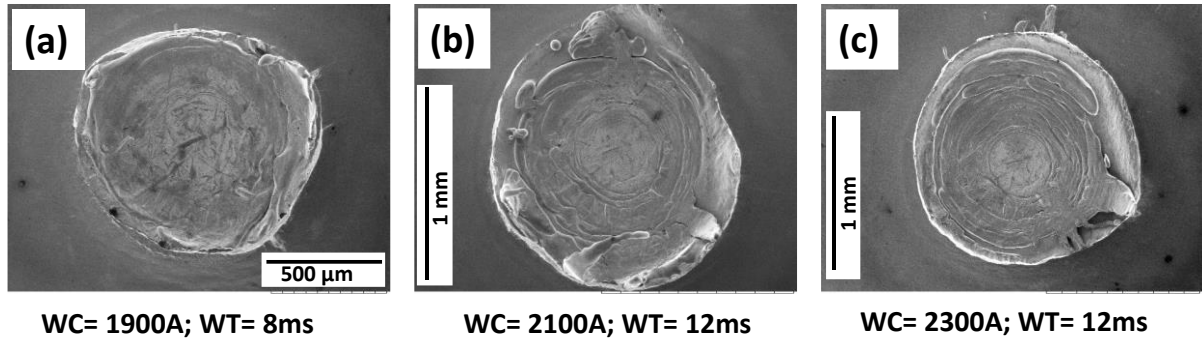


Fig. 12. Failure mode with process parameters (a) WC= 1900A, WT= 8ms (b) WC= 2100A, WT= 12ms and (c) WC= 2300A, WT= 12ms

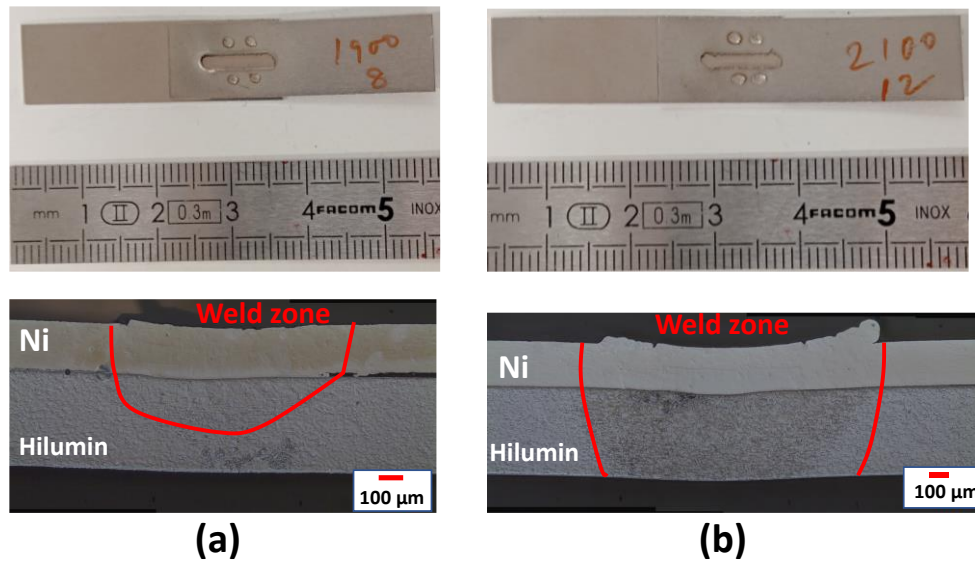


Fig. 13. Micro-RSW sample and their cross-sectional view at (a) WC= 1900 A; WT= 8 ms and (b) WC= 2100 A; WT= 12 ms

Also, no expulsion phenomenon has appeared in the limiting range of WC and WT. The combined effect of WC and WT is shown in **Fig. 11**. From **Fig. 11**, it was found that the ML was continuously increasing with WC and WT. A small increase in the maximum load was observed (**Table 6**) above the parameter combination of 2100 A weld current and 12 ms weld time. Also, the pull-out failure modes were observed for the parametric combination above 1800 A weld current and 8 ms weld time, as is illustrated in **Fig. 12**. Therefore, from **Table 6**, the optimized value of WC and WT required for the good-weld were (1900 – 2100 A) and (8 – 12 ms) respectively. Also, it can be observed from the weld cross-sectional view at the lower (WC= 1900 A; WT= 8 ms) and higher (WC= 2100 A; WT= 12 ms) value of the good-weld parameter set (**Fig. 13a** and **b**) that almost no bending of bottom sheet was obtained.

3.2.1. 90° peel load test at optimized parameter

It is important to evaluate the peel load which also defines the mechanical properties of the RSW joint. Because in the live cell joining configuration 90° peel load would also be applied. Hence, the peel load of the RSW joints of 0.2 mm Ni to 0.3/0.4 mm Hilumin was measured as per the set-up described in Section 2. The samples for the peel test were prepared at the optimized parameter determined from the 0.2 mm Ni to 0.3/0.4 mm Hilumin joints. The measured value of maximum peel load and nugget diameter with associated standard deviation is given in **Table 7**. **Fig. 14** shows the variation in maximum peel load and nugget diameter with optimized process parameters. The maximum nugget diameter and peel load was obtained for P2 (WC= 2000 A; WT= 12 ms) and P4 (WC= 2000 A; WT= 12 ms) for respective stack-up combinations. Because at a higher value of WC and WT, increase in heat input, the weld nugget size increased and subsequently produced deeper penetration depth and wider interface width consequentially more joint strength.

Table 7. 90° peel load and nugget diameter of 0.2 mm Ni to 0.3/0.4 mm Hilumin weld

Type	Process parameters	Maximum peel load (N) \pm SD	Nugget diameter (mm)
0.2 mm Ni to 0.3 mm Hilumin	WC= 1800A; WT= 8ms (P1)	125.51 \pm 11.23	0.82 \pm 0.05
	WC= 2000A; WT= 12ms (P2)	154.42 \pm 4.31	1.17 \pm 0.06
0.2 mm Ni to 0.4 mm Hilumin	WC= 1900A; WT= 8ms (P3)	147.57 \pm 11.36	0.96 \pm 0.04
	WC= 2100A; WT= 12ms (P4)	159.27 \pm 12.16	1.16 \pm 0.02

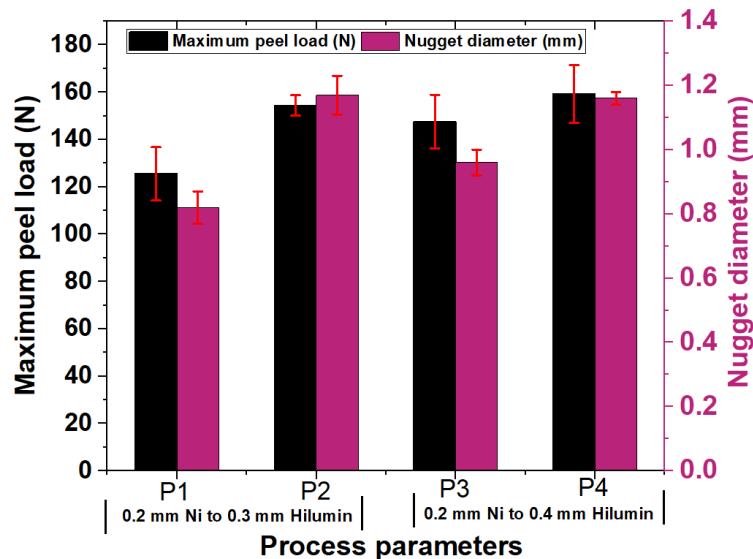


Fig. 14. Maximum peel load and nugget diameter at P1 (WC= 1800 A; WT= 8 ms), P2 (WC= 2000 A; WT= 12 ms), P3 (WC= 1900 A; WT= 8 ms) and P4 (WC= 2100 A; WT= 12 ms)

3.3. Analysis of electrical contact resistance

The specimens produced at optimized condition parametric conditions, as defined in section 3.2, were chosen for the resistance and temperature inspection. Each resistance test was performed three times and average values of resistance are reported. The electrical contact resistance was determined from the measured induced voltage across the micro-RSW joint using the voltage measuring pin as per the test set-up described in the experimentation (Section 2). **Fig. 15** shows the variation of resistance with time for 0.2 mm Ni to 0.3 mm Hilumin joints at process parameter P1 (WC= 1800 A; WT= 8 ms) and P2 (WC= 2000 A; WT= 12 ms) at 30 A current. The curves from the P1 and P2 parameters at 30 A current joints were almost congruent i.e., the insignificant effect of process parameters on resistance. The change in resistance was measured for 180 s at different amplitudes of current (i.e. 10 A, 20 A and 30 A) passed through the joints and the resistance after 180 s was shown in **Table 8**. Sufficient voltage measurements (i.e. total= 180, captured at 1s interval) could be taken within the test time to eliminate the effects of drift during the measurement cycle. From **Fig. 15**, it can be noted that after an initial fast rise the resistance only slowly increases within the period of applied current. When the current is increased the rate of rising in the resistance also increases. When the current was passed through the welded specimens, resistive heat loss generated heat increased the resistance of the joint and worked as a positive feedback loop [41]. As shown in **Table 8**, the resistance measured from the 0.2 mm Ni to 0.4 mm Hilumin is lower than the 0.2 mm Ni to 0.3 mm Hilumin joints for all amplitude of the current (10A, 20A and 30A).

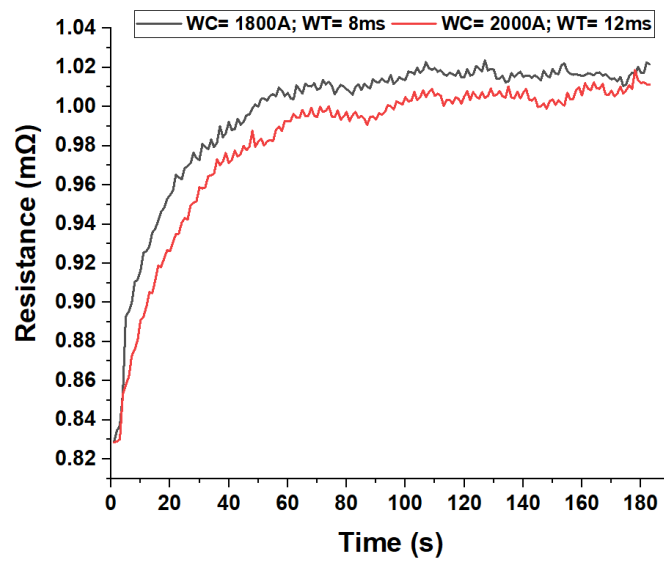


Fig. 15. Joint resistance of the 0.2 mm Ni to 0.3 mm Hilumin joints at P1 (WC= 1800 A; WT= 8 ms) and P2 (WC= 2000 A; WT= 12 ms) for 30A supply current

This is due to the fact that the resistance of a thin sheet is greater than the resistance of a thick sheet because a thin sheet has fewer electrons to carry the current. The relationship between resistance and the area of the cross-section of a sheet is inversely proportional [42]. For example, the lowest contact resistance was measured for the 0.2 mm Ni to 0.4 mm Hilumin weld at P4 parameters for 10A supplied current. Whereas, the maximum contact resistance was obtained for the 0.2 mm Ni to 0.3 mm Hilumin weld at P1 parameters for 30A supplied current. For 0.2 mm Ni tab to 0.3 mm Hilumin joints at the P1 parameter, the value of resistance at the beginning was around 0.82 m Ω irrespective of the applied current. At the end of 180 s of the current application, the resistance increased to 0.84 m Ω for 10 A, 0.89 m Ω for 20 A and 1.02 m Ω for 30 A, about 2.4%, 8.5% and 24% increase in resistance respectively. Similarly, for 0.2 mm Ni to 0.4 mm Hilumin weld at P4, the value of resistance at the beginning of the measurement was around 0.74 m Ω , and at the end of 180 s, the resistance increased close to 0.77 m Ω for 10 A current, 0.82 m Ω for 20 A current and 0.94 m Ω for 30 A (i.e. increased by about 4%, 11% and 27%) respectively. There is only a small change in resistance in each combination, a few microohms, but these values are too low to impact performance significantly. ~~Although the resistance variation is too small, a few micro ohms in each combination however these values are extremely low to have any significant performance impact.~~

Table 8. Joint resistance measurement of RSW joints

Supplied current (A)	Resistance after 180 s (m Ω)			
	0.2 mm Ni to 0.3 mm Hilumin		0.2 mm Ni to 0.4 mm Hilumin	
	WC= 1800A; WT= 8ms (P1)	WC= 2000A; WT= 12ms (P2)	WC= 1900A; WT= 8ms (P3)	WC= 2100A; WT= 12ms (P4)
10	0.84 \pm 0.01	0.80 \pm 0.02	0.78 \pm 0.03	0.77 \pm 0.03
20	0.89 \pm 0.01	0.89 \pm 0.03	0.81 \pm 0.02	0.82 \pm 0.01
30	1.02 \pm 0.03	1.01 \pm 0.01	0.95 \pm 0.03	0.94 \pm 0.02

3.4. Analysis of joint temperature rise

As electrical contact resistance is temperature dependent [43], it is necessary to describe the electrical resistances variation with respect to temperature. Due to the effect of Joule heating, the current-carrying micro-RSW samples warm up during the cycle of the current flow (i.e. representative of the charge-discharge cycle of the vehicle) [32]. The subsequent temperature rise was captured when currents of 10 A, 20 A and 30 A passed through the joints for 180 s each. **Fig. 16** shows the variation of rising in temperature with time for 0.2 mm Ni to 0.3 mm Hilumin joints at process parameter P1 (WC= 1800 A; WT= 8 ms) and P2 (WC= 2000 A; WT=

12 ms) at 30 A current. From **Fig. 16**, an insignificant effect of process parameters on temperature was observed. **Table 9** shows the rise in temperature of joints after 180 s at different amplitudes of current (i.e., 10 A, 20 A and 30 A). All results were measured from a room temperature of 24°C. The joint temperature rises for the 0.2 mm Ni to 0.4 mm Hilumin joints were lower than the 0.2 mm Ni to 0.3 mm Hilumin joints for all amplitudes of current. Although the top sheet (0.2 mm Ni) is common for both the joints but the electrical resistance for the 0.4 mm Hilumin is lower than the 0.3 mm Hilumin resultant lower resistance was obtained for the 0.2 mm Ni to 0.4 mm Hilumin combination [43]. For example, the temperature rise for 0.2 mm Ni tab to 0.3 mm Hilumin joints at P1 parameters, 26.1°C for 10 A, 37.4°C for 20 A and 63.6°C for 30 A, whereas the temperature rise for 0.2 mm Ni tab to 0.4 mm Hilumin joints at P3 parameter, 24°C for 10 A, 30.2°C for 20 A and 54.2°C for 30 A. Subsequently, the temperature and resistance were consistent with the effect of Joule heating (I^2R_{weld}). In this experiment, the welded coupons were exposed to the environment. In service, however, the welded joints would be enclosed within the confines of the battery box and expected to reach higher temperatures. Although commercial battery packs have an active or passive thermal management system (TMS), these are mainly designed to focus on the surface cooling of the cells [32]. The rise in joint temperature is recognized as one of the critical stress factors which could affect battery performance. Exposing the battery cells to high temperatures can accelerate ageing and promote solid electrolyte interface growth leading to premature failure [38, 39]. The results presented here indicate the significance of selecting the estimated value of pass current to minimize the detrimental effects of high joint temperature on Li-ion battery i.e., Li-ion battery can safely operate at 45°C [38, 44]. For example, the maximum rise in temperature for the 30 A current after 180 s for both the 0.2 mm Ni to 0.3 and 0.4 mm Hilumin joints were more than 45°C which is not suitable for Li-ion battery safe operation.

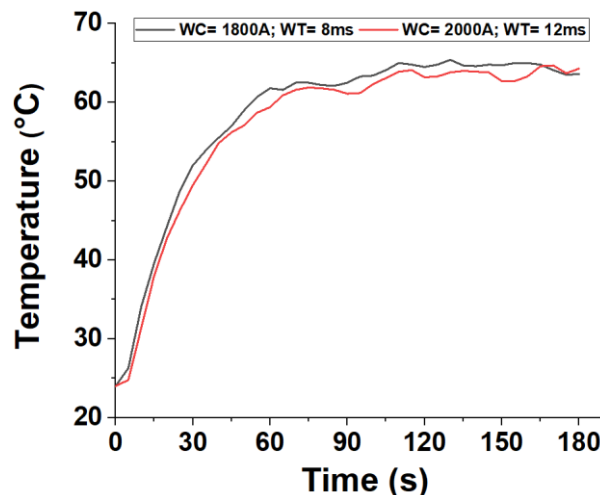


Fig. 16. Temperature measurement of the 0.2 mm Ni to 0.3 mm Hilumin at P1 (WC= 1800 A; WT= 8 ms) and P2 (WC= 2000 A; WT= 12 ms) for 30A supply current

Table 9. Rise in temperature at RSW joints

Supplied current (A)	Temperature after 180 s (°C)			
	0.2 mm Ni to 0.3 mm Hilumin		0.2 mm Ni to 0.4 mm Hilumin	
	WC= 1800A; WT= 8ms (P1)	WC= 2000A; WT= 12ms (P2)	WC= 1900A; WT= 8ms (P3)	WC= 2100A; WT= 12ms (P4)
10	26.1 ± 0.1	26.1 ± 0.2	24.0 ± 0	24.0 ± 0
20	37.4 ± 0.7	38.0 ± 0.5	30.2 ± 0.6	31.0 ± 0.5
30	63.6 ± 0.2	63.4 ± 0.8	54.2 ± 0.1	53.9 ± 0.8

3.5. Analysis of 18650 live cell welding

After completing the optimization for micro-RSW coupon samples of 0.2 mm Ni joined to 0.3/0.4 mm Hilumin, the optimized process parameters were used to weld the live cell positive and negative terminals. A pictorial view of the welded live cell at process parameters P2 and P4 is shown in **Fig. 17** showing two Ni tabs successfully welded. The weld quality of the tab to live cell was evaluated by 90° peel load. The measured value of 90° peel load obtained from the welded live cells was given in **Table 10**. It is evident from the 90° peel load value that high strength joints can be achieved for the tab to cell terminals. In addition, there was only a small difference (about 7%) in 90° peel load value was obtained between the 0.2 mm Ni to coupons (0.3/0.4 mm Hilumin) and live cell welding, which validated the applied approach and optimization method. Also, the cross-sectional images of tab to cell terminal welding were conducted to check the weld penetration. **Fig. 18(a)** and **(b)** showed a cross-sectional image of the tab to live cell negative terminal joints at parameters P1 and P2 respectively. Whereas, tab to positive terminal joints cross-section at parameter P3 and P4 was given in **Fig. 18(c)** and **(d)** respectively. It can be observed in **Fig. 18** that no bottom surface (negative and positive terminal) penetration and very small bending (especially in the case of P4, i.e., **Fig. 18d**) were obtained which is ideal for battery application because full penetration can produce cracks leading to electrolyte leakage or potential thermal run away. In addition, the weld quality was evaluated on the basis of the formation of the intermetallic phases in the micro-RSW joint as well. The weld joint conducted at parameter P4 has been selected for the IMC study because the thickness of the diffusion/fusion layer would be maximum because of P4 parameter has maximum WC (2100 A) and WT (12 ms) among all other parameters set (P1, P2 and P3) [45]. The SEM morphologies and enlarged image of the weld joints of the tab to positive terminal joints at parameter P4 are shown in **Fig. 19(a)**, **(b)** and **(c)** respectively. The energy dispersive

X-ray (EDX) analyser of the scanning electron microscope (SEM) was used to determine the composition of the compounds formed along the white lines L1, L2 and L3 shown in **Fig. 19(b)**. **Fig. 19(d)** shows the EDX line scan (i.e., L1, L2 and L3) results, which shows the changes in concentration of the Ni and Fe, and the weld interface layers were pointed out in the figure. A curve overlap means that intermetallic compounds were generated in the welded joints [32, 46]. For example, the curve overlapping (i.e., fluctuation in the Ni and Fe distribution curve) near the weld interface does not exist in **Fig. 19(d)**, indicating that no intermetallic compounds were formed. It is worth noting that the line scan analysis of the joint interface with L1, L2 and L3 shows that the atomic concentrations of Ni and Fe transition smoothly, and there is no transition plateau, indicating that only interdiffusion of the two elements occurs at the interface. At the same time, from enlarged pictures of weld (**Fig. 19c**), no obvious reaction layer was found at the interface, which confirms that the generation of intermetallic compounds at the Ni and Hilumin joint interface can be avoided under these experimental conditions (P1 - P4) [45].



Fig. 17. Live cell welding of the negative and positive terminal at P2 (WC= 2000 A; WT= 12 ms) and P4 (WC= 2100 A; WT= 12 ms) respectively

Table 10. 90° peel load of 18650 live cell terminals welding

Type	Process parameters	Maximum peel load (N) \pm SD
0.2 mm Ni to Negative terminal	WC= 1800A; WT= 8ms (P1)	119.93 \pm 5.58
	WC= 2000A; WT= 12ms (P2)	153.25 \pm 3.12
0.2 mm Ni to Positive terminal	WC= 1900A; WT= 8ms (P3)	137.73 \pm 3.93
	WC= 2100A; WT= 12ms (P4)	172.91 \pm 8.86

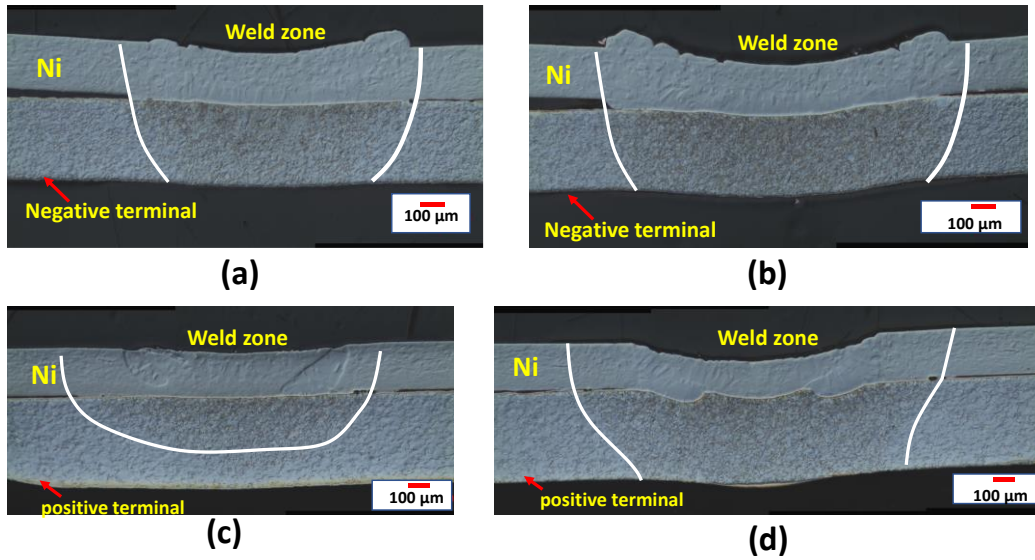


Fig. 18. Cross-sectional view of weld nuggets of tab to live cell joint at (a) WC= 1800 A; WT= 8 ms and, P1 (b) WC= 2000 A; WT= 12 ms, P2 (c) WC= 1900 A; WT= 8 ms, P3 and (d) WC= 2100 A; WT= 12 ms, P4

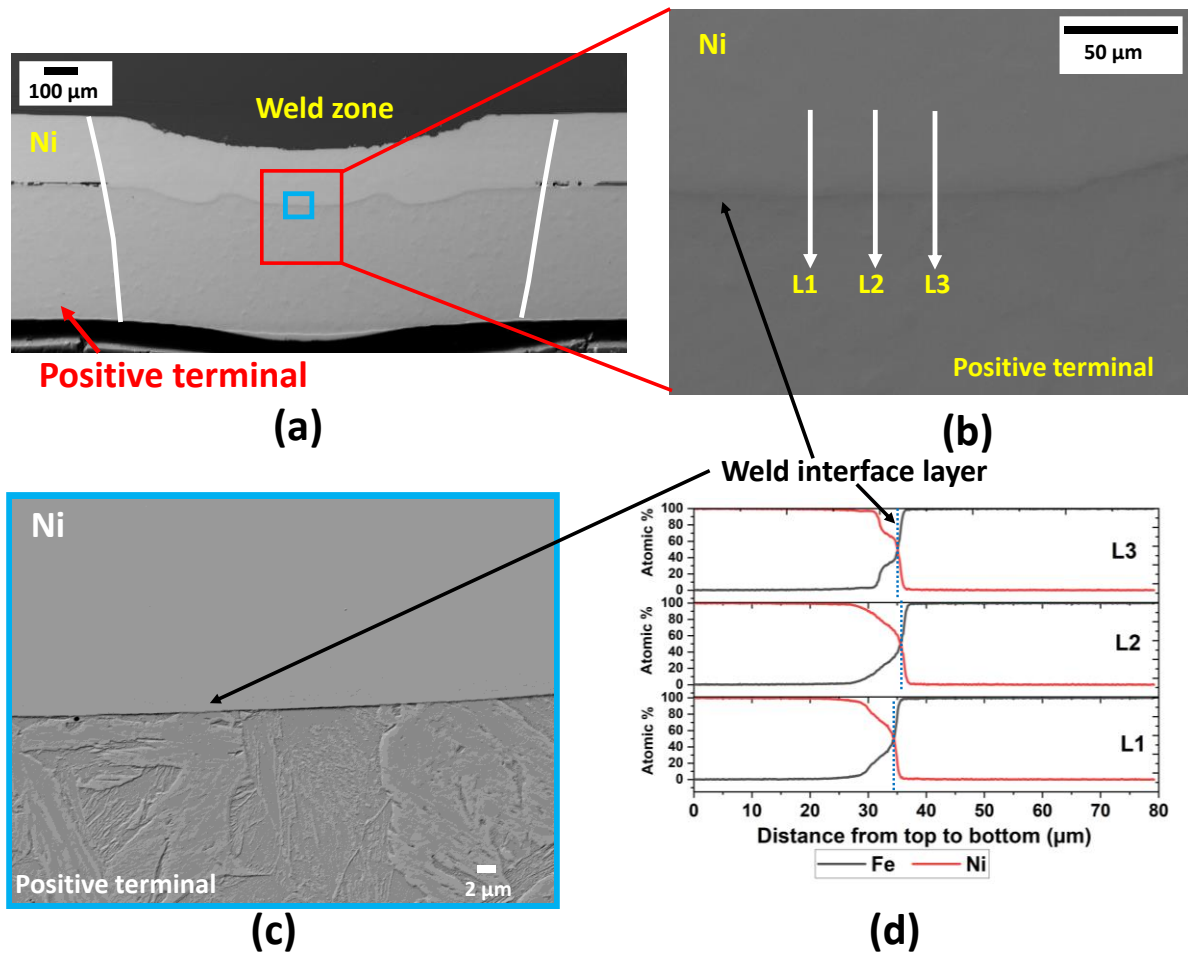


Fig. 19. (a) SEM image of the tab to positive terminal joints at WC= 2100 A; WT= 12 ms, P4

(b) enlarged view of the weld region (c) the enlarged view of blue box region in figure 19a and (d) EDX line scanning results of figure 19b

4. Conclusions

This work was conducted to study the effects of micro-RSW process parameters and optimize them. The obtained parameter setting can be used as a reference for welding 0.2 mm Ni connecting tabs on LG HG2 18650 Li-ion battery cells to create battery packs, in practice, if the geometry or materials of the connecting tab is changed, changes in parameter setting is likely to be necessary to achieve optimal welding results. From the foregoing analysis and discussion, the following conclusions were drawn:

- Micro-RSW has been demonstrated as a viable low production cost joining technique for joining the Ni connecting tabs and 18650 Li-ion cells for battery pack
- From ANOVA analysis, it was found that the weld current had the most significant and positive influence on the maximum/peak load followed by weld time. Whereas the process parameters like squeeze time, pre-heat current, pre-heat time, dwell time and hold time had insignificant effect on the maximum load.
- The optimized process parameters limits for the maximum load (maximization) were evaluated by full factorial design of experiment and weld current of (1800 – 2000A), (1900 – 2100A) and weld time of (8 – 12 ms) were required for the 0.2 mm Ni tab to negative and positive cell terminals joining, respectively. Additionally, the fixed parameters were squeeze time of 50 ms, rise and fall time of 1 ms, pre-heat time of 2.5 ms, dwell time of 3 ms, hold time of 100 ms and pre-heat current of 1200 A.
- In the lap-shear examination, the maximum load obtained from the four nuggets joints was about two times more than the joints having two nuggets.
- The specimens were tested at 10A, 20A, and 30A input current through each specimen for 180s. The increase in resistance is higher at 30A as compared to 10A and 20A considering the temperature rise due to resistive heating.
- Due to Joule heating, the joint temperature rise was acquired when a current was conducted through the joints. The maximum temperature variation range for both 0.2 mm Ni to 0.3/0.4 mm Hilumin joints was between 53.9°C to 64.6°C with 30A current passed for 180 sec and 30.2°C to 38°C at 20A and 24°C to 26.1°C at 10A. The thermal results are in line with electrical results verifying the proportionality between increased resistance and corresponding temperature rise.

- From joint temperature rise measurement, the estimated value of pass current can be estimated to minimize the detrimental effects of high joint temperature i.e., Li-ion battery can safely operate.
- No intermetallic compounds were generated at the Ni and Hilumin joint interface under the optimized parametric conditions.

A systematic study was conducted in this work to optimize the micro-RSW process parameters for connecting the Ni tab to 18650 cells in a battery pack. Further, the optimized welded cells can be used for charging, discharging, internal resistance and capacity analyses as future work.

Declarations

Funding: This research is supported by the WMG High-Value Manufacturing Catapult and TVS Motor Company, India under a joint research program for automotive energy storage.

Conflicts of interest/Competing interests: The authors declare that they have no known competing financial interests or personal relationships that could have appeared to influence the work reported in this paper.

Availability of data and material: Not applicable

Code availability: Not applicable

Ethics approval: The author obliged all the rules regarding the ethics in publication.

Consent to participate: Not applicable

Consent for publication: All the authors are consent regarding publication immediately after acceptance.

Authors' contributions: Not applicable

References

1. R. Faria, P. Moura, J. Delgado, AT de Almeida, 'A sustainability assessment of electric vehicles as a personal mobility system', Energy Conversion and Management 61 (2012) 19-30.
2. Nesbit M, Fergusson M, Colsa A, Ohlendorf J, Hayes C, Paquel K, Schweitzer J-P. Comparative study on the differences between the EU and US legislation on emissions in the automotive sector. Brussels; 2016.
3. <https://hubis.co.kr/en/ev/battery/> (Accessed 01/07/2022).

4. J.-M. Tarascon, M. Armand, 'Issues and challenges facing rechargeable lithium batteries', *Nature* 414 (2001) 359-367.
5. A. Das, D. Li, D. Williams, D. Greenwood, 'Joining technology for automotive battery systems manufacturing', *World Electric Vehicle Journal* 9 (2018) 1-13.
6. U.F. Shaikh, A. Das, A. Barai, I. Masters, 'Electro-thermo-mechanical behaviours of laser joints for electric vehicle battery interconnects', *Electric Vehicles International Conference (EV)* (2019) 1-6.
7. J.H. Cha, H.W. Choi, 'Characterization of dissimilar aluminum-copper material joining by controlled dual laser beam', *The International Journal of Advanced Manufacturing Technology* 119 (2022) 1909–1920.
8. S. Grabmann, J. Kriegler, F. Harst, F.J. Guntur, M.F. Zaeh, 'Laser welding of current collector foil stacks in battery production—mechanical properties of joints welded with a green high-power disk laser', *The International Journal of Advanced Manufacturing Technology* 118 (2022) 2571–2586.
9. A. Das, D. Li, D. Williams, D. Greenwood, 'Weldability and shear strength feasibility study for automotive electric vehicle battery tab interconnects', *Journal of the Brazilian Society of Mechanical Sciences and Engineering* 41 (2019) 54.
10. A. Ratner, W. Wood, M. Chowanietz, N. Kumar, R. Patel, P. Hadlum, A. Das, I. Masters, 'Laser doppler vibrometry for evaluating the quality of welds in Lithium-Ion supercells', *Energies* 15 (2022) 4379.
11. S.S. Lee, T.H. Kim, S.J. Hu, W.W. Cai, J.A. Abell, 'Joining technologies for automotive lithium-ion battery manufacturing: a review', *ASME 2010 International Manufacturing Science and Engineering Conference* 1 (2010) 541–9.
12. M.J. Brand, P.A. Schmidt, M.F. Zaeh, A. Jossen, 'Welding techniques for battery cells and resulting electrical contact resistances', *Journal of Energy Storage* 1 (2015) 7–14.
13. M. Masomtob, R. Sukondhasingha, J. Becker, D.U. Sauer, 'Parametric study of spot welding between Li-ion battery cells and sheet metal connectors', *Engineering Journal* 21 (2017) 457-473.
14. A. Risdiyanto, U. Khayam, N.A. Rachman, M. Arifin, 'Experimental and simulation studies of thermal distribution on modified connector of Li-ion battery for electric vehicles application', *International Journal of Electrical and Computer Engineering* 6 (2016) 2064–72.
15. <https://amadaweldtech.com/glossary/glosselectrodeconfig> (Accessed 01/07/2022).
16. <https://www.dnkpowers.com/why-18650-battery-explode/> (Accessed 01/07/2022).

17. S.J. Dong, G.P. Kelkar, Y. Zhou, 'Electrode sticking during micro-resistance welding of thin metal sheets', *IEEE Transactions on Electronics Packaging Manufacturing* 25 (2002) 355-361.
18. V.R. Rikka, S.R. Sahu, A. Roy, S.N. Jana, D. Sivaprahasam, R. Prakash, R. Gopalan, G. Sundararajan, 'Tailoring micro resistance spot welding parameters for joining nickel tab to inner aluminium casing in a cylindrical lithium-ion cell and its influence on the electrochemical performance', *Journal of Manufacturing Processes* 49 (2020) 463–471.
19. K.J. Ely, Y. Zhou, 'Microresistance spot welding of Kovar, steel, and nickel', *Science and Technology of Welding and Joining* 6 (2001) 63-72.
20. N. Kumar, S. Dhara, I. Masters, A. Das, 'Substituting resistance spot welding with flexible laser spot welding to join ultra-thin foil of Inconel 718 to thick 410 steel', *Materials* 15 (2022) 3405.
21. A.S. Baskoro, H. Muzakki, G. Kiswanto, W. Winarto, 'Effects of micro resistance spot welding parameters to weld joint quality on aluminum thin plate AA 1100', *International Journal of Technology* 8 (2017) 1306-1313.
22. S. Liu, X. Liu, R. Doua W. Zhou, Z. Wen, L. Liu, 'Experimental and simulation study on thermal characteristics of 18,650 lithium–iron–phosphate battery with and without spot–welding tabs', *Applied Thermal Engineering* 166 (2020) 114648.
23. <https://www.tatasteeleurope.com/sites/default/files/1462%20TATA%20Hilumin.pdf> (accessed 01/07/2022).
24. A. Das, R. Beaumont, I. Masters, P. Haney, 'Macro-modelling of laser micro-joints for understanding joint strength in electric vehicle battery interconnects', *Materials* 14 (2021) 3552.
25. K. Mahmud, S.P. Murugan, Y. Cho, C. Ji, D. Nam, Y.-Do Park, 'Geometrical degradation of electrode and liquid metal embrittlement cracking in resistance spot welding', *Journal of Manufacturing Processes* 61 (2021) 334-348.
26. W. Mazur, A. Kyriakopoulos, N. Bott, D. West, 'Use of modified electrode caps for surface quality welds in resistance spot welding', *Journal of Manufacturing Processes* 22 (2016) 60-73.
27. https://www.mipalloy.com/dispersioned_strengthened_copper.html (Accessed 01/07/2022).
28. D.W. Lee, O. Tolochko, C.J. Choi, B.K. Kim, 'Aluminium oxide dispersion strengthened copper produced by thermochemical process', *Powder Metallurgy* 45 (2002) 267–270.

29. P. Schmitz, J.B. Habedank, M.F. Zaeh, 'Spike laser welding for the electrical connection of cylindrical lithium-ion batteries', *Journal of Laser Applications* 30 (2018) 1-7.
30. P.A. Schmidt, M. Schweier, M. F. Zaeh, 'Joining of lithium-ion batteries using laser beam welding: Electrical losses of welded aluminum and copper joints', in *International Congress on Applications of Lasers & Electro-Optics (ICALEO)*, Anaheim, 23–27 September 31 (2012) 915–923.
31. Q. Zhang, R. C. Sekol, C. Zhang, Y. Li, B. E. Carlson, 'Joining lithium-ion battery tabs using solder-reinforced adhesive', *Journal of Manufacturing Science and Engineering* 141 (2019) 044502-7.
32. N. Kumar, I. Masters, A. Das, 'In-depth evaluation of laser-welded similar and dissimilar material tab-to-busbar electrical interconnects for electric vehicle battery pack', *Journal of Manufacturing Processes* 70 (2021) 78–96.
33. S. Hu, A.S. Haselhuhn, Y. Ma, Y. Li, B.E. Carlson, Z. Lin, 'Comparison of the resistance spot weldability of AA5754 and AA6022 aluminum to steels', *Welding Journal* 99 (2020) 224-38.
34. T. Solchenbach, P. Plapper, W. Cai, 'Electrical performance of laser braze-welded aluminum–copper interconnects', *Journal of Manufacturing Processes* 16 (2014) 183–189.
35. M. Pouranvari, H.R. Asgari, S.M. Mosavizadeh, P.H. Marashi, M. Goodarzi, 'Effect of weld nugget size on overload failure mode of resistance spot welds', *Science and Technology of Welding and Joining* 12 (2007) 217–25.
36. X. Sun, E.V. Stephens, R.W. Davies, M.A. Khaleel, D.J. Spinella, 'Effects of fusion zone size on failure modes and static strength of aluminum resistance spot welds', *Welding Journal* 83 (2004) 308s–18s.
37. A.M. Pereira, J.M. Ferreira, A. Loureiro, J.D.M. Costa, P.J. Bártolo, 'Effect of process parameters on the strength of resistance spot welds in 6082-T6 aluminium alloy', *Materials and Design* 31 (2010) 2454–2463.
38. A. Das, T.R. Ashwin, A. Barai, 'Modelling and characterisation of ultrasonic joints for Li-ion batteries to evaluate the impact on electrical resistance and temperature raise', *Journal of Energy Storage* 22 (2019) 239-248.
39. A. Das, A. Barai, I. Masters, D. Williams, 'Comparison of tab-to-busbar ultrasonic joints for electric vehicle Li-ion battery applications', *World Electric Vehicle Journal* 10 (2019) 55.

40. M. Baumann, L. Wildfeuer, S. Rohr, M. Lienkamp, 'Parameter variations within Li-Ion battery packs—Theoretical investigations and experimental quantification' *Journal of Energy Storage* 18 (2018) 295–307.
41. A. Das, I. Masters, P. Haney, 'Modelling the impact of laser micro-joint shape and size on resistance and temperature for Electric Vehicle battery joining application', *Journal of Energy Storage* 52 (2022) 104868.
42. M. Núñez, 'Generalized Ohm's law and geometric optics: Applications to magnetosonic waves', *International Journal of Non-Linear Mechanics* 110 (2019) 21-25.
43. E. Schrüfer, [Elektrische Messtechnik], Hanser, 221-223 (1990).
44. H. Niu, C. Chen, D. Ji, L. Li, Z. Li, Y. Liu, X. Huang, 'Thermal-runaway propagation over a linear cylindrical battery module', *Fire Technology* 56 (2020) 2491–2507.
45. X. Gu, C. Sui, X. Di, Z. Meng, K. Zhu, C. Chu, 'Effect of welding energy on performance of Cu/Ti joints obtained by ultrasonic welding', *Journal of Jilin University (Engineering and Technology Edition)* 50 (2020) 1669-1676.
46. X. Zhao, Z. Shi, C. Deng, Y. Liu, X. Li, 'The effect of laser offset welding on microstructure and mechanical properties of 301L to TA2 with and without Cu intermediate Layer', *Metals* 10 (2020) 1138.